Glass production rate in an electric melter: melting rate correlation and primary foam stability

Pavel Hrma[1], Pavel Ferkl[*2], Richard Pokorný[3], Albert A. Kruger[4]

[1] AttainX, Support Services Contractor to the Office of River Protection, U.S. Department of Energy, Richland, WA 99354, United States of America

[2] Pacific Northwest National Laboratory, Richland, WA 99354, United States of America

[3] Laboratory of Inorganic Materials, University of Chemistry and Technology Prague, Prague 6, 166 28, Czech Republic

[4] U.S. Department of Energy, Office of River Protection, Richland, WA 99354, United States of America

Abstract

Waste loading and melting rate are major factors determining the lifecycle of nuclear waste disposal by vitrification in electric melters in which the heat to the cold cap is delivered from the melt pool. One of the crucial parameters that affect the rate of melting is the temperature at which the primary foam collapses at the cold cap bottom. Apart from the transient glass-forming melt viscosity, primary foam stability is affected by the shear stress imposed by the flow in the melt pool and the presence of residual solid particles.

Introduction

The lifecycle of nuclear waste disposal by vitrification depends significantly on both glass formulation [1, 2] and the rate at which the melters are producing the waste glass. Considering the large number of waste components and the complex process of melter feed conversion to molten glass, optimizing the melting rate is a formidable task for any single nuclear waste and even more so for ~55000 waste compositions to be vitrified in Hanford [3].

Factors affecting the glass production rate, including the waste treatment, the choice of glass-forming and modifying additives, melting technology, and melter operation parameters, are optimized using scaled melter runs [4-6] and mathematical modeling [7, 8]. Still, far from simulating the full complexity of the vitrification process, mathematical modeling succeeded in representing the cold cap (reacting melter feed floating on the melt pool in the waste glass melter) [9] (Fig. 1) that consists of the core layer, in which melter feed is heated to the conversion onset temperature, the open porosity reaction layer, and the primary foam layer, in which enough transient glass-forming melt has been produced to close the pores, trapping the evolving gases. The cold cap bottom is where the primary foam is collapsing, releasing gas into cavities carried away by the melt circulating under the cold cap [10]. The cold cap bottom temperature is a crucial link between the melter CFD model and the cold cap model. Its value depends on the primary foam stability, which is the main topic of this contribution.

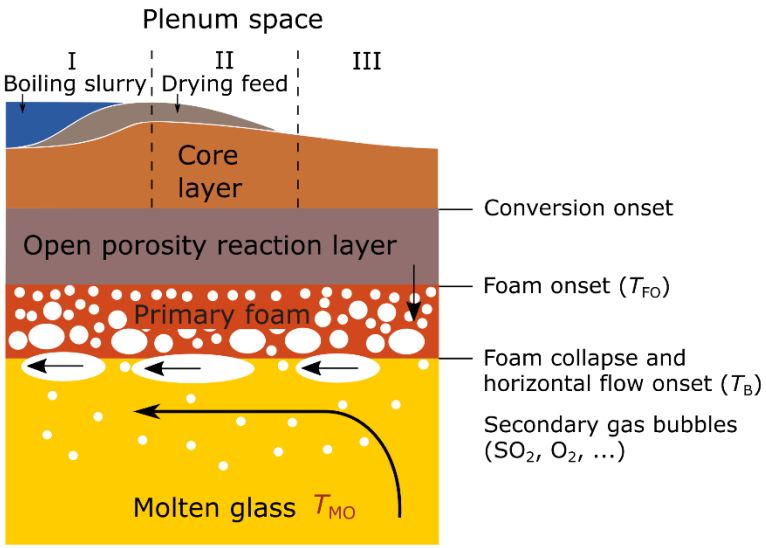

Fig. 1. Three major layers of the cold cap floating on molten glass. In slurry-fed melters, the core layer surface is partly covered by boiling slurry (I), drying wet melter feed (II), and dry melter feed (III) that alternate as slurry overflows to the lowest areas.

The glass production rate

Since nearly all heat enters the cold cap bottom from the melt pool, the glass production rate per cold-cap area, j, can be expressed as

$$j = h(T_{\mathrm{MO}} - T_{\mathrm{B}})/\Delta H, \tag{1}$$

where h is the heat transfer coefficient, T_{MO} is the melter operating temperature (nearly uniform within the well-stirred melt pool [8]), T_{B} is the cold cap bottom temperature, and ΔH is the melter feed-to-glass melt conversion heat. The value of T_{B} is not accessible to direct measurement and is estimated using various tests and criteria [11, 12].

The heat transfer coefficient is

$$h = \lambda/\delta_T, \tag{2}$$

where λ is the glass melt thermal conductivity and δ_T is the thermal boundary layer thickness. In mostly opaque glasses, such as high-level waste (HLW) glasses that contain Fe_2O_3, NiO, Cr_2O_3, and/or MnO, in which natural convection is too weak, the glass production rate is enhanced with pneumatic stirring by gas bubbling that suppresses δ_T.

Generally, the heat transfer coefficient is a function of the Reynolds and Prandtl numbers,

$$h = \zeta Re^{\gamma} \mathrm{Pr}^{\delta}, \tag{3}$$

where ξ, γ, and δ are parameters depending on the pattern of the velocity and temperature fields in the melt pool.

The Reynolds number is defined as

$$\mathrm{Re} = z_{\mathrm{M}} \varrho u/\eta, \tag{4}$$

where u is the bubbling gas flow rate, z_M is the cold cap distance from the bubbler orifice, and ϱ is the density, and the Prandtl number is

$$\mathrm{Pr} = \eta c_p/\lambda\,, \tag{5}$$

where η is the viscosity and c_p is the specific heat. The value of λ is highly uncertain because of numerous bubbles and solid particles that scatter and absorb thermal radiation in the thermal boundary layer. Fortunately, Eq. (1) was successfully fitted to a broad range of data for j from 5 to 25 g m^{-2} s^{-1} in the form of the melting rate correlation (MRC) [13]:

$$j = \xi \mathrm{Re}^{\gamma}(T_{\mathrm{MO}} - T_{\mathrm{B}})/\Delta H, \tag{6}$$

where ξ and γ are the only adjustable parameters (for HLW glasses, ξ = 337 W m^{-2} K^{-1} and $\gamma \approx$ ½ [13]).

Primary Foam Stability

Primary foam collapses by the massive coalescence of bottom foam cells through the combination of viscosity decrease and stretching the cell walls below the critical thickness, as continuous glass evolution and thermal expansion increase the foam porosity, and the shear stress deforms the bottom foam cells.

The shear stress is imposed on the primary foam bottom by forced convection: foam cells become slanted and, as shown in Fig. 2, foam cell lamellae are stretched and thinned.

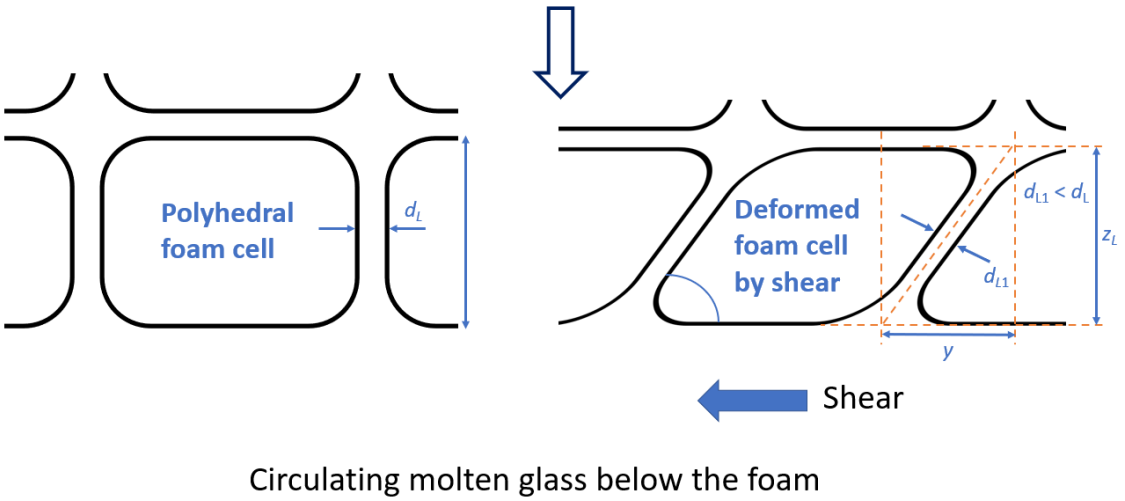

Fig 2. After undeformed foam cells (left) reach foam the layer bottom, they are slanted by shear (right).

Assuming, for simplicity, that the critical lamella thickness is indirectly proportional to the transient melt viscosity:

$$\eta_{\mathrm{MB1}} = \eta_{\mathrm{MB}} d_L/d_{\mathrm{L1}}, \tag{7}$$

where d_{L} and d_{L1} are the original and the stretched critical lamella thickness, respectively, and η_{MB} and η_{MB1} are the corresponding transient melt viscosity at the cold cap bottom. For small differences $\Delta\eta = \eta_{\mathrm{MB1}} - \eta_{\mathrm{MB}}$, assuming $\eta \sim \exp(T)$, the cold cap bottom temperature difference, $\Delta T_{\mathrm{B}} = T_{\mathrm{B}} - T_{\mathrm{B1}}$, can be approximated as:

$$\Delta T_{\mathrm{B}} = b_{\eta}\log(1 + \Delta\eta/\eta), \tag{8}$$

where b_{η} is a constant.

Provided that the volume of the bottom foam cells remains constant, and that the lamella volume is not changing during stretching,

$$\frac{d_{\mathrm{L}}}{d_{\mathrm{L1}}} = \sqrt{1 + \left(\frac{y}{z_{\mathrm{L}}}\right)^2}, \tag{9}$$

where *y* is the transverse displacement relative to the upper foam cells and z_{L} is the vertical lamella length (Fig. 2).

Neglecting gravity drainage, which operates in surface foams [14, 15], but does not significantly affect primary foam, and disregarding the surface forces that oppose the sharpening of the chamfer angle $\beta = \arccos\left(\frac{d_{\mathrm{L}}}{d_{\mathrm{L1}}}\right)$ (Fig. 2), the slanting, y/z_{L}, is caused by the foam side bottom shear rate, v'_{FB}, as

$$y/z_{\mathrm{L}} = v'_{\mathrm{FB}} t_{\mathrm{L}}\,, \tag{10}$$

where t_{L} is the lamella survival time. Considering that

$$t_{\mathrm{L}} = z_{\mathrm{L}}/v_z, \tag{11}$$

where v_z is the transient melt velocity, and that

$$v_z = j/\rho_{\mathrm{F}}, \tag{12}$$

where ρ_{F} is the primary foam density, we obtain

$$t_{\mathrm{L}} = z_{\mathrm{L}}\rho_{\mathrm{F}}/j, \tag{13}$$

By the balance of momentum,

$$\eta_{\mathrm{MB}} v'_{\mathrm{MB}} = \eta_{\mathrm{FB}} v'_{\mathrm{FB}}, \tag{14}$$

where v'_{MB} is the melt side bottom shear and η_{FB} is the foam side viscosity.

The relationship between the shear rate under the cold cap and the bubbling rate can be approximated as

$$v'_{\mathrm{MB}} = b_0 + b_1 u. \tag{15}$$

By Eqs. (8) to (15),

$$\Delta T_{\mathrm{B}} = \frac{1}{2} b_{\eta} \log\left[1 + \left(\frac{\eta_{\mathrm{MB}}}{\eta_{\mathrm{FB}}} \frac{v'_{\mathrm{MB}} z_{\mathrm{L}} \varrho_{\mathrm{F}}}{j}\right)^2 (b_0 + b_1 u)^2\right]. \tag{16}$$

The feed-to-glass conversion reactions oppose the change in ΔT_B [16]. Using a linear approximation, Eq. (16) can be generalized as

$$\Delta T_{\mathrm{B}} = -p_Q Q_{\mathrm{B}} + p_u u, \tag{17}$$

where Q_{B} is the heat flux from the melt pool to the cold cap bottom and

$$p_u = \frac{\partial T_\mathrm{B}}{\partial u}\Big|_{u=u_0} = -b_1 b_\eta \frac{b_0 + b_1 u}{\left(\frac{\eta_\mathrm{FB} j}{\eta_\mathrm{MB} z_\mathrm{L} \varrho_\mathrm{F}}\right)^2 + (b_0 + b_1 u)^2}. \quad (18)$$

Example. Fig. 3 shows the ΔT_B vs. u function for the Al-19 melter feed. For the Al-19 melter feed, v'_FB = 0.016 s^{-1}. With j = 950 kg m^{-2} s^{-1} and ρ_F = 400 kg m^{-3} [16], $v_z = j/\rho_F$ = 2.75 × 10^{-2} mm s^{-1}. With z_L = 3 mm [17, 18], Eq. (13) yields t_L = 109 s. Let the lamella of d_L = 100 μm thins to d_L1 = 50 μm (β = 60, Fig. 2). For the Arrhenius approximation, $\log(\eta/\eta_\infty) = B/T$ with B = 1.775×10^4 K, we get b_η = 280 K^{-1}. With η_FB = 126 Pa s [19] and v'_MB = 0.05 s^{-1}; Eq. (14) yields η_MB1 = 80 Pa s. Based on a CFD model [8], b_0 = 0.011 s^{-1} and b_1 = 0.0078 m^{-1}. According to [19], p_Q = 9.51 × 10^{-3} K W^{-1} m^2. For u_0 = 5 m s^{-1}, Eq. (18) yields p_u = 32.8 K s m^{-1}.

Although the derivation of Eq. (16) was based on a specific foam structure geometry, the foam shearing effect will operate whether the primary foam is spherical (a bubbly melt) or cellular.

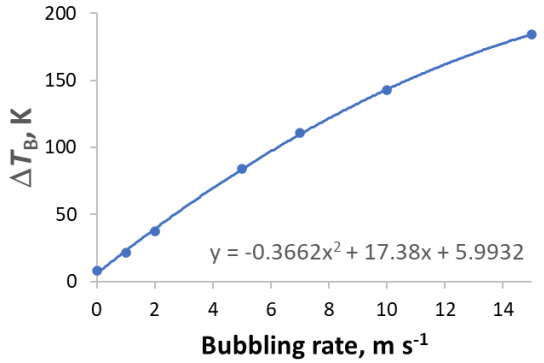

Fig. 3. Effect of bubbling rate on the cold cap bottom temperature drop, ΔT_B, Eq. (16).

Other effects

The transient melt composition is changing by the continuing reactions and diffusion-controlled homogenization. The critical thickness of lamellae depends on the fraction and position of the dispersed particles, such as silica, spinel, or zircon. Dissolving remnants of silica increase the melt viscosity in their vicinity [20]. As Fig. 4 illustrates, in the lamellae, where the low-viscosity silica-poor regions are the weak points, silica particles destabilize foam, but stabilize it in Plateau borders, where the high viscosity hinders the melt inflow from cell walls.

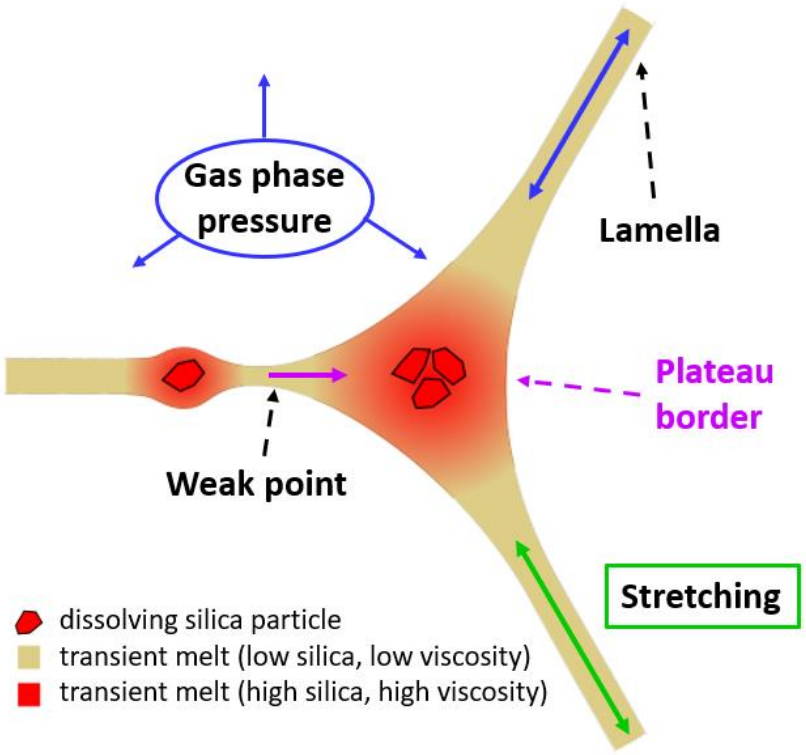

Fig. 4. Plateau border with liquid lamellae and silica inclusions.

Concluding Remark

The cold cap bottom temperature, a melting-rate-controlling parameter, depends on the primary foam stability, which, apart from the transient glass-forming melt viscosity, is affected by the shear stress imposed by the flow in the melt pool, and the presence of residual solid particles, an effect to be investigated. A term for gas bubbling rate was added to the relationship between ΔT_{B} and the conversion rate.

Acknowledgments

The authors acknowledge financial support provided by the U.S. Department of Energy (DOE) Waste Treatment and Immobilization Plant Project, and by the Czech Ministry of Education, Youth and Sports Project No. LUAUS23062. Pacific Northwest National Laboratory is operated by Battelle for the DOE under contract DE-AC05-76RL01830.

References

[1] P. Hrma, J.V. Crum, D.J. Bates, P.R. Bredt, L.R. Greenwood, H.D. Smith, Journal of Nuclear Materials 345 (2005) 19-30. https://doi.org/10.1016/j.jnucmat.2005.03.026.
[2] X. Lu, J.D. Vienna, J. Du, Journal of the American Ceramic Society (2023). https://doi.org/10.1111/jace.19333.
[3] X. Lu, D.-S. Kim, J.D. Vienna, Nuclear Engineering and Design 385 (2021) 111543. https://doi.org/10.1016/j.nucengdes.2021.111543.
[4] I.L. Pegg, Phys Today 68(2) (2015) 33-39. https://doi.org/10.1063/Pt.3.2687.

[5] D.R. Dixon, D. Kim, M.J. Schweiger, C.M. Fischer, C.D. Lukins, P. Hrma, Nuclear Engineering and Design 367 (2020) 110782. https://doi.org/10.1016/j.nucengdes.2020.110782.
[6] D.R. Dixon, M.A. Hall, J.B. Lang, D.A. Cutforth, C.M. Stewart, W.C. Eaton, Ceramics International (2021). https://doi.org/10.1016/j.ceramint.2021.08.102.
[7] M.K. Choudhary, B. Purnode, A.M. Lankhorst, A.F.J.A. Habraken, International Journal of Applied Glass Science 9 (2018) 218-234. https://doi.org/10.1111/ijag.12286.
[8] A.W. Abboud, D.P. Guillen, P. Hrma, A.A. Kruger, J. Klouzek, R. Pokorny, International Journal of Applied Glass Science 12 (2021) 233-244. https://doi.org/10.1111/ijag.15863.
[9] P. Ferkl, P. Hrma, J. Kloužek, A.A. Kruger, R. Pokorný, International Journal of Applied Glass Science (2023) 1-15. https://doi.org/10.1111/ijag.16645.
[10] R. Pokorny, P. Hrma, Journal of Nuclear Materials 429 (2012) 245-256. https://doi.org/10.1016/j.jnucmat.2012.06.013.
[11] N. Ueda, M. Vernerová, J. Kloužek, P. Ferkl, P. Hrma, T. Yano, R. Pokorný, Journal of the American Ceramic Society 104 (2021) 34-44. https://doi.org/10.1111/jace.17406.
[12] P. Ferkl, P. Hrma, A. Abboud, D.P. Guillen, J. Khawand, I. Kopal, M. Kohoutková, M. Vernerová, J. Kloužek, M. Hall, A.A. Kruger, R. Pokorný, Journal of Non-Crystalline Solids 579 (2022) 121363. https://doi.org/10.1016/j.jnoncrysol.2021.121363.
[13] S. Lee, P. Ferkl, R. Pokorny, J. Klouzek, P. Hrma, W.C. Eaton, A.A. Kruger, Journal of the American Ceramic Society 103 (2020) 5573-5578. https://doi.org/10.1111/jace.17281.
[14] P. Hrma, Journal of Colloid and Interface Science 134(1) (1990) 161-168. https://doi.org/10.1016/0021-9797(90)90262-M.
[15] L. Pilon, R. Viskanta, Chemical Engineering and Processing: Process Intensification 43 (2004) 149-160. https://doi.org/10.1016/S0255-2701(03)00012-6.
[16] P. Ferkl, P. Hrma, A. Abboud, D.P. Guillen, M. Vernerova, J. Klouzek, M. Hall, A.A. Kruger, R. Pokorny, International Journal of Applied Glass Science (2022). https://doi.org/10.1111/ijag.16615.
[17] W.H. Harris, D.P. Guillen, J. Klouzek, R. Pokorny, T. Yano, S. Lee, M.J. Schweiger, P. Hrma, Journal of the American Ceramic Society 100 (2017) 3883-3894. https://doi.org/10.1111/jace.14895.
[18] S.A. Luksic, R. Pokorny, P. Hrma, T. Varga, E.L. Rivers, A.C. Buchko, J. Klouzek, A.A. Kruger, Ceramics International 47 (2021) 15807-15818. https://doi.org/10.1016/j.ceramint.2021.02.153.
[19] J. Marcial, J. Chun, P. Hrma, M. Schweiger, Environmental Science & Technology 48 (2014) 12173-12180. https://doi.org/10.1021/es5018625.
[20] M.J. Schweiger, P. Hrma, C.J. Humrickhouse, J. Marcial, B.J. Riley, N.E. TeGrotenhuis, Journal of Non-Crystalline Solids 356(25-27) (2010) 1359-1367. https://doi.org/10.1016/j.jnoncrysol.2010.04.009.